Editors' Suggestion

Enhancing the sensitivity of single-microwave-photon detection with bandwidth tunability

Louis Pallegoix,[1] Jaime Travesedo,[1] Alexandre S. May,[1,2] Léo Balembois,[1] Denis Vion,[1] Patrice Bertet,[1,*] and Emmanuel Flurin[1,†]

[1] *Université Paris-Saclay, CEA Paris-Saclay, CNRS, SPEC, 91191 Gif-sur-Yvette, France*
[2] *Alice & Bob, 53 Boulevard du Général Martial Valin, 75015 Paris, France*

(Received 13 January 2025; revised 29 July 2025; accepted 10 November 2025; published 23 April 2026)

We report on the characteristics of a microwave photon-counter device based on a superconducting transmon qubit. Its design is similar to that described by Balembois *et al.* [Phys. Rev. Appl. **21**, 014043 (2024)], which achieved a sensitivity of 10^{-22} W/$\sqrt{\text{Hz}}$, but with an additional bandwidth-tuning circuit that permits tuning the detection bandwidth over an order of magnitude to optimize the efficiency and noise level of the device. As a result of this feature and improvements in device fabrication, a power sensitivity of 3×10^{-23} W/$\sqrt{\text{Hz}}$ is reached. We confirm the high performance of the device by measuring single-spin microwave fluorescence.

DOI: 10.1103/dbqj-qld5

I. INTRODUCTION

Single-photon detection has long been a fundamental tool in quantum technologies, with well-established applications in the optical domain, ranging from fluorescence microscopy [1–4] to quantum communication [5] and boson sampling [6]; however, extending single-photon detection into the microwave regime presents significant challenges. The energy of microwave photons—of the order of μeV—is several orders of magnitude lower than that of optical photons, requiring detectors to operate at cryogenic temperatures to suppress thermal noise and reduce the background thermal photon population.

Despite these challenges, single-microwave-photon detectors (SMPDs) have emerged as critical tools for advancing quantum sensing and information processing. Their ability to detect individual microwave photons has opened possibilities for a wide range of applications, including the detection of weak incoherent microwave emitters, such as electron spins in solids [7–9], and even searches for hypothetical dark-matter particles [10,11]. SMPDs also hold potential for primary thermometry at low temperatures [12] and for use in quantum illumination protocols [13]. Moreover, these detectors can play a key role in quantum information processing [14–16], enabling heralded entanglement between superconducting qubits [17], improving qubit readout schemes [18], and facilitating the generation of robust quantum states [19].

Various SMPD designs have been proposed and implemented, with most relying on superconducting qubits [7,17,20–32], quantum dots [33,34] or bolometric detectors [35]. These devices have demonstrated promising results, achieving sensitivities ranging from 10^{-21} to 10^{-22} W/$\sqrt{\text{Hz}}$ at microwave frequencies; however, there remain limitations in terms of bandwidth, detection efficiency, and dark count rates that must be addressed to further enhance their performance.

In this work, we present an enhanced version of the SMPD introduced in Ref. [36], which is based on a superconducting qubit and a four-wave mixing (4WM) process. The design integrates a frequency-tunable Purcell filter, providing control over the detection bandwidth. Since the thermal noise power is proportional to the detection bandwidth, this tunability significantly reduces thermal noise and decreases the dark count rate to 30 s^{-1}, improving the overall detector performance. Additionally, advancements in the fabrication process have led to an extended qubit relaxation time (T_1), which in turn enhances the detection efficiency to 0.8. As a result of these improvements, the detector achieves a power sensitivity of 3×10^{-23} W/$\sqrt{\text{Hz}}$, representing a significant advancement over previous designs. We confirm the improved sensitivity of the SMPD by detecting the microwave fluorescence from a single spin.

*Contact author: patrice.bertet@cea.fr
†Contact author: emmanuel.flurin@cea.fr

Published by the American Physical Society under the terms of the Creative Commons Attribution 4.0 International license. Further distribution of this work must maintain attribution to the author(s) and the published article's title, journal citation, and DOI.

II. SMPD PRINCIPLE OF OPERATION

A. Device design

The SMPD device [see Figs. 1(a) and 1(b)] consists of a transmon qubit (mode q, frequency ω_q), capacitively coupled to two harmonic oscillator modes, called the buffer (mode b, frequency ω_b) and the waste (mode w, frequency ω_w). The buffer is connected to the input line of the device through another resonator at frequency ω_{pb}. The latter serves as Purcell filter to decouple the qubit from the input line, while also setting the effective buffer energy coupling rate $\kappa_{b,c}$. The total energy-loss rate of the buffer resonator is $\kappa_b = \kappa_{b,c} + \kappa_{b,i}$, where $\kappa_{b,i}$ represents the internal losses of the buffer. The waste is connected to an output line through another Purcell filter, at frequency ω_{pw}, with a rate κ_w. Other relevant parameters are the qubit energy-relaxation time T_1 and equilibrium excited-state population, $p_{\mathrm{th},q}$, which varies with the qubit temperature T, in the $T \ll \hbar\omega/k_B$ limit, as $p_{\mathrm{th},q} = 1/(e^{\hbar\omega_q/k_BT} - 1)$. In this formula, T is not necessarily the cryostat base temperature, as various heating effects (due to infrared radiation in particular) may lead to a higher effective qubit temperature.

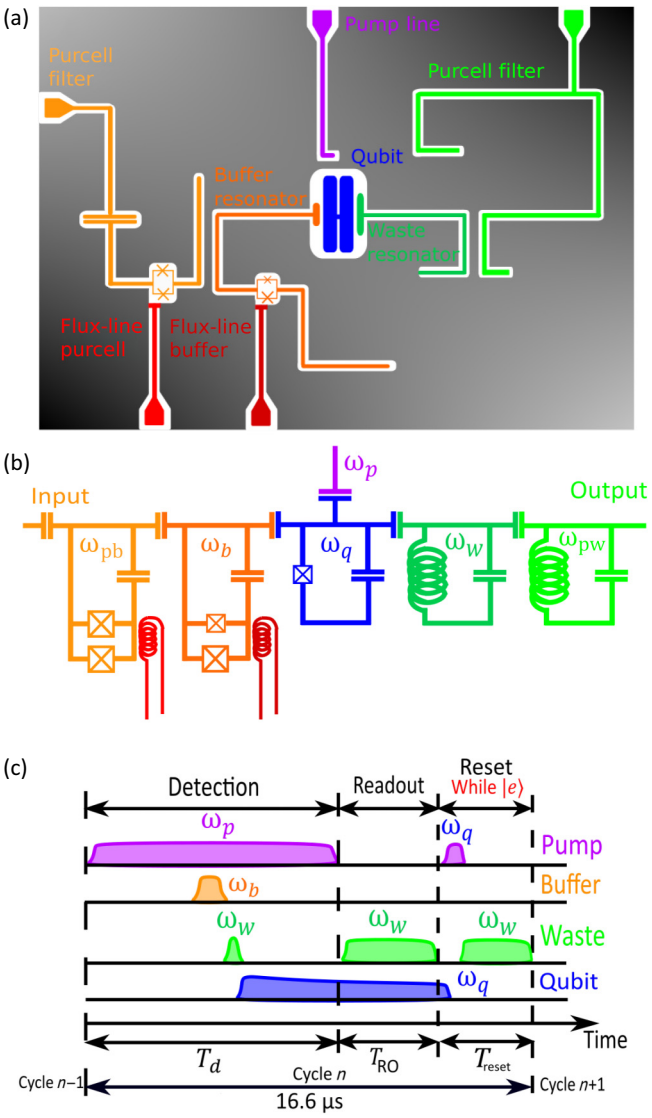


FIG. 1. Overview of the device. (a) Global layout of the SMPD. (b) Lumped-element scheme of the SMPD. The colors of the different resonators are in accordance with their colors on the chip scheme. Note: The buffer SQUID is asymmetrical. (c) Operation cycle of the SMPD. During the detection step (duration T_d), the pump is switched on; a photon arriving in the buffer mode is converted into a photon in the waste, which quickly decays, and a qubit excitation, which decays in a characteristic time $T_1 \gg T_d$. Dispersive readout is performed through the waste resonator in time T_{RO}. If the qubit is found in $|e\rangle$, a π pulse is applied, followed by qubit readout, and reapplication of the reset if it is found in $|e\rangle$. This conditional reset step lasts T_{reset}. The whole cycle lasts 16.6 µs (assuming one reset cycle).

For optimal operation as an energy detector, both the frequency and bandwidth of the device need to be matched to the source of interest, be it a spin [8,36] or a dark-matter candidate [37]. Frequency tuning is achieved by inserting a superconducting quantum interference device (SQUID) into the buffer mode, resulting in a buffer frequency $\omega_b(\phi_b)$ that depends on the flux threading the buffer SQUID loop, ϕ_b. An asymmetric SQUID is purposely chosen to minimize sensitivity to flux noise. Bandwidth tuning is achieved by inserting a second SQUID into the Purcell filter mode, resulting in a buffer coupling rate $\kappa_{b,c}(\phi_{\mathrm{pb}})$ that depends on the flux threading the Purcell SQUID loop, ϕ_{pb}. This SQUID is symmetric to maximize the bandwidth-tuning range.

B. Four-wave mixing

The working principle of photon detection relies on a 4WM process that maps the presence or absence of a photon onto the state of the transmon qubit. The nonlinear element is provided by the qubit Josephson junction. The 4WM is activated by a microwave signal (called the pump, frequency ω_p) of amplitude ξ_0, applied to the qubit via a pump line connected capacitively to the qubit (see Fig. 1). When the pump frequency approximately satisfies the relation $\omega_b + \omega_p = \omega_q + \omega_w - \chi_w$, the dominant process is described by the Hamiltonian

$$H_{\mathrm{4WM}} = \sqrt{\chi_b \chi_w}(\xi_0 b q^\dagger w^\dagger + \xi_0^* b^\dagger q w), \tag{1}$$

where χ_b (χ_w) is the qubit dispersive coupling to the buffer (waste) mode [20]. This Hamiltonian reversibly converts a buffer and pump photon into a qubit excitation and waste photon. Dissipation of the waste photon into the output line ensures that the process is irreversible; nonetheless, the qubit remains excited long enough to be readout subsequently, and it can thus be used as a flag that frequency conversion occurred.

An approximate description is obtained by eliminating the qubit degree of freedom, yielding an effective Hamiltonian $H_{\text{eff}} = g_{4\text{WM}} b w^\dagger + \text{H.c.}$ with $g_{4\text{WM}} = \sqrt{\chi_b \chi_w}\xi_0$. This describes the parametric coupling between the buffer and waste modes, similar to the Josephson parametric converter, for instance. Assuming that $\kappa_{b,i} \ll \kappa_{b,c}$, the efficiency of frequency conversion under this process is $\eta_{4\text{WM}} = 4C/(1+C)^2$, where $C = (4\chi_b\chi_w|\xi_0|^2)/\kappa_w\kappa_b$ is the system cooperativity. Unit efficiency is reached when $C = 1$. Physically, this occurs when the frequency-conversion rate $4|g_{4\text{WM}}|^2/\kappa_w$ is equal to the input resonator coupling rate, κ_b. This condition can always be achieved by adjusting the pump frequency and amplitude (see Appendix A for more details).

C. Cyclic operation

The SMPD is operated cyclically. A cycle consists of three successive steps: detection, readout, and reset [see Fig. 1(c)]. During the detection step, which lasts T_d, the pump drive is simply switched on, with suitable amplitude and frequency for maximum frequency conversion. In the next step, dispersive qubit readout is achieved via the waste resonator by measuring the reflected field quadratures of a microwave tone in a time T_{RO}. We define the readout fidelity $\mathcal{F}_{\text{RO}}^{|e\rangle} < 1$ as the probability of measuring the qubit in the excited state after a π pulse.

In the third step, the qubit is reset into its ground state by applying a π pulse conditioned to the outcome of the previous readout being the excited state. This efficiently resets the qubit into its ground state, with a probability that can be even lower than the thermal-equilibrium qubit excited-state probability [36]. Note that the duration of the reset step T_{reset} varies from cycle to cycle due to its conditional nature. The detector duty cycle η_{cycle} is defined as the average value of $T_d/(T_d + T_{\text{RO}} + T_{\text{reset}})$.

III. FIGURES OF MERIT

In this section, we describe in some detail the processes that limit the performance of the device as an energy detector. This performance is captured by the power sensitivity S, defined as the power that can be detected with unit signal-to-noise ratio in 1-s integration time [36]:

$$S = \hbar\omega_b \frac{\sqrt{\alpha}}{\eta_{\text{SMPD}}}. \tag{2}$$

In this formula, η_{SMPD} is the overall detection efficiency of the SMPD and α is the average number of counts per second when no signal is sent to the device. The latter can be separated in two contributions $\alpha = \alpha_{\text{err}} + \alpha_{\text{th}}$, α_{err} being the false-positive events and α_{th} being the counts due the detection of thermal photons in the input line. In what follows, we address each of these three quantities, with the goal of maximizing η_{SMPD} while minimizing α_{err} and α_{th}.

A. Detection efficiency

A photon can be missed if:

(1) it is spectrally filtered by the detector;
(2) the 4WM efficiency is not 1;
(3) the qubit relaxes back in its ground state during the detection step;
(4) qubit excited-state readout fails;
(5) the photon hits the detector during the readout or reset steps.

Therefore, the probability that a photon in the input line at frequency ω gives rise to a count is

$$\eta_{\text{SMPD}}(\omega) = \eta_\omega \eta_{4\text{WM}} \eta_q \mathcal{F}_{\text{RO}}^{|e\rangle} \eta_{\text{cycle}}, \tag{3}$$

where the detector frequency response function is approximated by a Lorentzian of width κ_d (the detector linewidth) such that $\eta_\omega = 1/(1 + [2(\omega - \omega_b)/\kappa_d]^2)$. The qubit efficiency $\eta_q = (T_1/T_d)(1 - \text{e}^{-(T_d/T_1)})$ can be approximated by $1 - T_d/2T_1$ in the limit $T_d \ll T_1$ [36]. To maximize η_{SMPD}, T_d should be optimized to maximize the duty cycle while keeping the cycle time well below T_1 to avoid relaxation of the qubit before readout.

B. Dark count rate

The dark count rate α_{err} is the number of counts detected per unit time, even though no photon was present in the input line. It has two contributions, $\alpha_{\text{err}} = \alpha_q + \alpha_p$. First, the qubit can be found in the excited state despite the active reset procedure. This is due to the relaxation toward the thermal-equilibrium value $p_{\text{th},q}$, which takes place during the detection window with a characteristic time T_1 [36], giving rise to $\alpha_q = p_{\text{th},q}(T_d/T_1)(1/(T_d + T_{\text{RO}} + T_{\text{reset}}))$ (assuming that the active reset works perfectly, otherwise an offset must be added to that expression). The other contribution α_p is due to heating brought by the pump. Note that the readout errors causing the ground state to be erroneously detected as the excited state are negligible because we purposely choose a detection threshold that minimizes this effect.

C. Thermal counts

Thermalizing the microwave field at millikelvin temperatures is well known to be a difficult task because of vanishing thermal conductivity and the large attenuation needed in the input lines. This results in an effective field temperature that is often significantly larger than the cryostat base temperature, and in our case, in the presence of a finite flux of thermal photons at the SMPD input, causing

a thermal count rate of thermal origin

$$\alpha_{\rm th} = \frac{1}{2\pi}\int_{-\infty}^{\infty} \bar{n}_{{\rm th},b}\eta_{\rm SMPD}(\omega)\,d\omega, \tag{4}$$

where $\bar{n}_{{\rm th},b} = \frac{1}{e^{\frac{\hbar\omega_b}{k_B T}}-1}$ is the number of photons per mode assuming that the field is at temperature T. Because $\kappa_d \ll \omega_b$, we get

$$\alpha_{\rm th} = \frac{\bar{n}_{{\rm th},b}\kappa_d\eta_{\rm SMPD}(\omega_b)}{4}. \tag{5}$$

Due to the tunable bandwidth of our device, we are able here to test the predicted proportionality between noise and detector bandwidth, as will be seen below.

IV. MEASUREMENTS

A. Device characterization

The SMPD resonators are measured with a vector network analyzer (VNA). Each resonance is fitted to determine the resonator frequency and linewidth. The results of these fits are reported in Table I.

Figure 2(a) shows $\omega_b(\phi_b)$ for several values of $\phi_{\rm pb}$. The buffer tuning range is narrow (60 MHz), and the curve is well fitted by a sinusoid [38], from which we deduce a ratio of 15 between the Josephson-junction critical currents of the asymmetric SQUID. Little crosstalk between ϕ_b and $\phi_{\rm pb}$ is observed, as evidenced by the weak dependence of $\omega_b/2\pi$ on $\phi_{\rm pb}$.

From the fits of the buffer resonance curves, we extract $\kappa_{b,i} = 2.2\times10^5$ s^{-1}, and $\kappa_{b,c}$, the internal loss and coupling rates, respectively. Figure 2(c) shows $\kappa_{b,c}/2\pi$ as a function of the detuning from the Purcell, $\omega_b - \omega_{\rm pb}$. A large tuning range is observed, ranging from approximately 10 kHz up to approximately 3 MHz. The tuning curve is identical for all values of buffer-resonator frequency [see Fig. 2(c)]. The buffer is overcoupled over a large parameter range (corresponding to $\kappa_{b,c} \gg \kappa_{b,i}$), which is desirable for SMPD operation, as buffer internal losses further reduce $\eta_{\rm 4WM}$ [36].

Qubit readout is performed at the waste-resonator frequency when the qubit is in the excited state, $\omega_w - \chi_w$,

TABLE I. Measured resonator frequencies and linewidths. The Purcell filter of the buffer and the buffer itself are tunable over the indicated interval. The buffer linewidth depends on the Purcell frequency, as shown in Fig. 2.

Resonator	Frequency (GHz)	Linewidth
Buffer Purcell	$\omega_{\rm pb}/2\pi \in [7.26; 7.78]$	20 MHz
Buffer	$\omega_b/2\pi \in [7.70; 7.76]$	See Fig. 2
Qubit	$\omega_q/2\pi = 6.533$	16 kHz
Waste	$\omega_w/2\pi = 8.475$	1.75 MHz
Waste Purcell	$\omega_{\rm pw}/2\pi \approx 8.39$	400 MHz

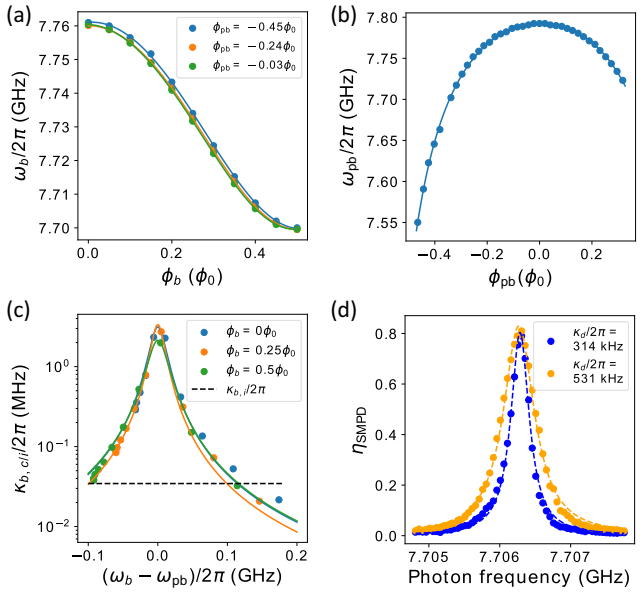


FIG. 2. Tunability curves. (a) Solid circles are the measured frequency of the buffer resonator, ω_b, as a function of the flux bias applied to its SQUID, Φ_b, for several values of $\Phi_{\rm pb}$ (blue is $-0.45\Phi_0$, orange is $-0.24\Phi_0$, green is $-0.03\Phi_0$). The solid lines are sinusoidal fits, yielding the asymmetry between the buffer SQUID junctions. (b) Full blue circles are the measured frequency of the Purcell filter, $\omega_{\rm pb}$, as a function of the flux bias sent to its SQUID $\Phi_{\rm pb}$. The solid line is a fit assuming a symmetric SQUID. (c) Full circles show the measured coupling rate of the buffer resonator to the 50-Ω line as a function of its detuning from the Purcell filter, $\omega_b - \omega_{\rm pb}$, for three different values of Φ_b: blue for $\Phi_b = 0$, orange for $\Phi_b = 0.25\Phi_0$, green for $\Phi_b = 0.5\Phi_0$. The dashed line shows the internal losses of the buffer, $\kappa_{b,i}$. The solid lines are Lorentzian fits to data of the same color. We can see that $\kappa_b/2\pi$ rise above 3 MHz at zero detuning and fall below $\kappa_{b,i}$ when the detuning exceeds 100 MHz in absolute value. (d) Full circles are the measured SMPD efficiency, $\eta_{\rm SMPD}$, as a function of signal frequency ω, for $\kappa_b/2\pi = 170$ kHz (blue) and 280 kHz (orange). Dashed lines are Lorentzian fits, yielding the SMPD bandwidth $\kappa_d/2\pi$, equal to 314 and 531 kHz, respectively.

to minimize the chances of exciting it out of the ground state and causing unwanted dark counts, with a readout duration $T_{\rm RO} = 0.8$ μs. Readout histograms are shown in Appendix A, yielding the readout fidelity $\mathcal{F}_{\rm RO}^{|e\rangle} = 0.87$ and equilibrium excited-state population $p_{{\rm th},q} = 8.5\times10^{-4}$. Note that the readout fidelity is significantly lower than those found in recent experiments, which reach values close to 0.99 [39]. This is because the waste-resonator parameters (χ_w and κ_w) are optimized for the 4WM process and not for qubit readout, which would require a larger value of κ_w, reaching approximately χ_w [39] (see Tables I and II). The qubit lifetime is $T_1 = 70$ μs (see Appendix A), and the coherence time measured under a Ramsey sequence is $T_2^* = 20$ μs. The dispersive shifts χ_b and χ_w are reported in Table II. Active reset is performed as explained in Sec. II C [36].

TABLE II. Measured dispersive shifts induced by the qubit to its neighboring resonators.

Resonator	Cross-Kerr to qubit
Buffer	$\chi_b/2\pi = 3.5$ MHz
Waste	$\chi_w/2\pi = 16$ MHz

B. Four-wave-mixing tuning

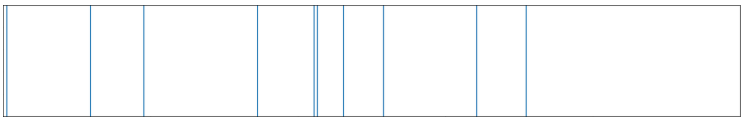
The 4WM condition is found by sending a pump tone at frequency ω_p together with a signal at frequency ω into the SMPD input, followed by qubit readout. Sweeping ω_p and ω, the 4WM condition is identified by an enhanced qubit excited state when the signal is present, which vanishes when it is switched off; the pump power is then tuned to reach unit cooperativity (see Appendix A).

C. Cyclic operation: Detector bandwidth and dark counts

We now turn to operation of the SMPD in cyclic mode. The detection step duration is set to $T_d = 15$ μs. When no photon is sent to the device, the qubit is most often in the ground state at the end of the sequence, implying that no reset is needed and that the average cycle duration is very close to $T_d + T_{\mathrm{RO}} = 15.8$ μs, yielding a duty cycle $\eta_{\mathrm{cycle}} = 0.95$. From Eq. (3), we expect η_{SMPD} to reach 0.74.

The experimental η_{SMPD} is measured by counting the number of clicks detected over a 1-s integration time, at the same time that a calibrated signal is sent to the SMPD input. The signal power is calibrated using the qubit as a detector (see Ref. [36] and Appendix B). The result is plotted as a function of input frequency ω in Fig. 2(d). The maximum efficiency reaches $\eta_{\mathrm{SMPD}} = 0.8$. This is even slightly higher than the predicted value, which implies in particular that the 4WM efficiency $\eta_{4\mathrm{WM}}$ is very close to 1. Fitting $\eta_{\mathrm{SMPD}}(\omega)$ with a Lorentzian, we obtain the detector bandwidth κ_d. Two curves are shown, obtained for two different values of κ_b. The maximum efficiency is unchanged, but the detector bandwidth is changed according to κ_b. This confirms that the SMPD bandwidth can be adjusted by tuning κ_b via the Purcell filter frequency. We measure $\kappa_d/2\pi = 315$ kHz for $\kappa_b/2\pi = 170$ kHz, and $\kappa_d/2\pi = 530$ kHz for $\kappa_b/2\pi = 280$ kHz, thus confirming the approximate relation $\kappa_d \simeq 2\kappa_b$ (see Appendix A).

TABLE III. Photon-counting traces taken under different conditions. First line: the mixing-chamber temperature is 10 mK and the pump is off, yielding α_q. Second line: the mixing-chamber temperature is 10 mK and the pump is switched on, but it is detuned by 20 MHz from the 4WM condition, yielding $\alpha_{\mathrm{err}} = \alpha_q + \alpha_p$. Third line: the mixing-chamber temperature is 10 mK, and the pump is on and in the 4WM condition, yielding $\alpha_{\mathrm{err}} + \alpha_{\mathrm{th}}$. Three following lines: the mixing-chamber temperature is increased, and the count rate rises accordingly, as detailed in Fig. 3.

Temperature (mK)	Pump state	$\kappa_d/2\pi$ (kHz)	One-second click sequence	Click rate (s^{-1})
10	Off	Not relevant		8
10	Detuned	Not relevant		10
10	Tuned	170		31
50	Tuned	170		344
60	Tuned	170		621
90	Tuned	170		3614

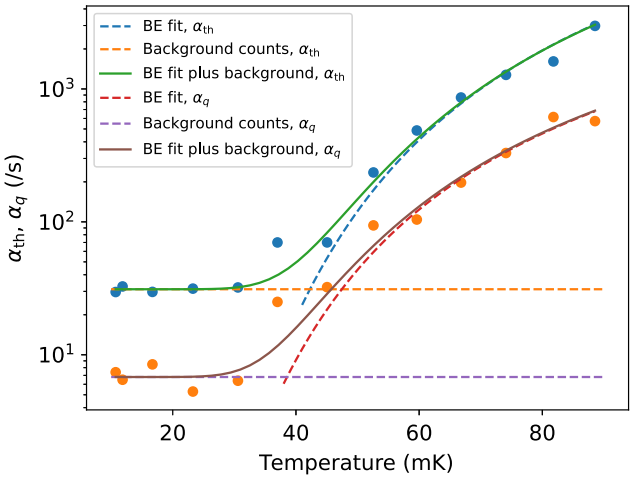


FIG. 3. Measured α_{th} (blue full circles) and α_q (orange full circles) as a function of the cryostat's temperature T, for a detection bandwidth $\kappa_d/2\pi = 170$ kHz. The solid green line is a fit of α_{th} to $\alpha_{\text{th},0} + K_{\text{th}}\bar{n}_{\text{th},b}(T)$, yielding $\alpha_{\text{th},0} = 31\ \text{s}^{-1}$ and $K_{\text{th}} = 2 \times 10^5\ \text{s}^{-1}$. The solid brown line is a fit of α_q to $\alpha_{q,0} + K_q p_{\text{th},q}(T)$, yielding $\alpha_{q,0} = 7\ \text{s}^{-1}$ and $K_q = 2.2 \times 10^4\ \text{s}^{-1}$. The dashed lines are the separated Bose-Einstein and constant components of the respective fits.

Dark counts are measured by recording photon-counting traces in the absence of any input signal (see Table III, where the detector bandwidth was $\kappa_d/2\pi = 170$ kHz). To obtain the various contributions to the dark counts, the traces are systematically measured with the pump off (yielding α_q), with the pump on and detuned by 20 MHz (yielding $\alpha_q + \alpha_p = \alpha_{\text{err}}$), and with the pump on and tuned to the 4WM conditions (yielding $\alpha = \alpha_{\text{err}} + \alpha_{\text{th}}$). At 10 mK, we obtain $\alpha_q = 8\ \text{s}^{-1}$, $\alpha_p = 2\ \text{s}^{-1}$, and $\alpha_{\text{th}} = 21\ \text{s}^{-1}$. Combining this with the measured efficiency, we obtain a power sensitivity $S = 3 \times 10^{-23}\ \text{W}/\sqrt{\text{Hz}}$, a factor of 3 better than the previous state of the art [36], which corresponds to an order of magnitude gain in measurement time.

Time traces are similarly measured by varying the cryostat temperature T. The values of α_q and α_{th} are shown as a function of T in Fig. 3. The qubit contribution increases with temperature because of the higher excited-state probability at equilibrium; it is well fitted by $\alpha_{q,0} + K_q p_{\text{th},q}(T)$, with $\alpha_{q,0} = 7\ \text{s}^{-1}$ and $K_q = 2.2 \times 10^4\ \text{s}^{-1}$. The value of K_q is slightly larger than the predicted $(T_d/T_1)(1/(T_d + T_{\text{RO}} + T_{\text{reset}}))$ (see Sec. III B), which is $1.4 \times 10^4\ \text{s}^{-1}$, possibly because of a reduction in T_1 at higher temperature. The thermal contribution also increases with temperature; it is well fitted by $\alpha_{\text{th},0} + K_{\text{th}}\bar{n}_{\text{th},b}$, with $\alpha_{\text{th},0} = 31\ \text{s}^{-1}$, and $K_{\text{th}} = 2 \times 10^5\ \text{s}^{-1}$. This value is in quantitative agreement with the expected $\eta_{\text{SMPD}}\kappa_d/4 = 2.1 \times 10^5\ \text{s}^{-1}$, thus providing an independent confirmation of the efficiency estimate reported earlier.

The equilibrium qubit excitation (without active reset) $p_{\text{th},q}$ at 10 mK translates into an effective qubit temperature of 42 mK. The thermal photon rate $\alpha_{\text{th},0}$ measured at 10 mK translates into a mean photon number per mode of 1.5×10^{-4} and thus to an effective temperature of 40 mK. This is higher than the mean photon number expected from our line attenuation, which we estimate to be below approximately 2×10^{-5}. Our results therefore confirm the well-known difficulty of thermalizing microwave fields and modes to temperatures much lower than approximately 40 mK, possibly due to the difficulty of perfectly thermalizing microwave components. It is interesting to note that SMPD devices are ideally well suited to studying this phenomenon, which represents a major issue for superconducting quantum computers.

D. Dependence on detection bandwidth

We finally study the SMPD figures of merit as a function of detection bandwidth at the lowest temperature of 10 mK. We measure the maximum value of $\eta_{\text{SMPD}}(\omega)$ and α as a function of κ_d (see Fig. 4). We observe that η_{SMPD} increases with κ_d, although the dependence is very weak as soon as the SMPD bandwidth is above 250 kHz. This is expected because the measurements are performed with a monochromatic tone. The reduction in efficiency at the lowest value of κ_d may be attributed to the contribution of internal buffer losses, as well as possible transient effects that effectively shorten the detection time T_d.

The false-positive rate α, however, scales linearly with κ_d, as expected from Eq. (5). The fitted slope is 1.6×10^{-5}, in agreement with the expected $\eta_{\text{SMPD}}\bar{n}_{\text{th},b}/4$, yielding a thermal mode occupation $\bar{n}_{\text{th},b} = 0.8 \times 10^{-4}$, slightly

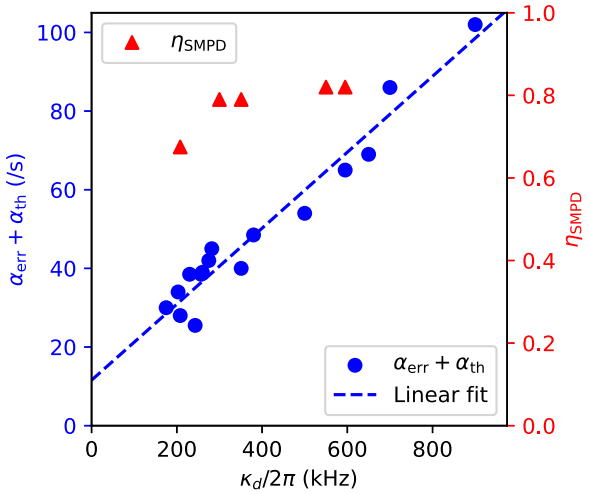


FIG. 4. The blue full circles are the measured total dark counts, $\alpha_{\text{err}} + \alpha_{\text{th}}$, as a function of SMPD bandwidth κ_d. The dashed line is a linear fit, with slope 1.5×10^{-5} and intercept $11.6\ \text{s}^{-1}$. The red triangles show the measured efficiency at resonance, η_{SMPD}.

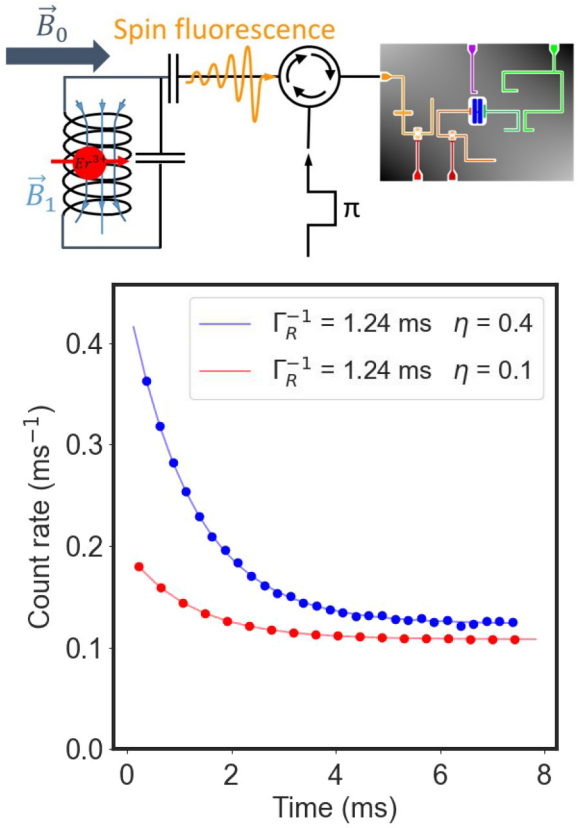


FIG. 5. Microwave fluorescence of individual Er^{3+} electron spins in a $CaWO_4$ host crystal matrix at 10 mK, detected by the SMPD reported here operated with $\kappa_d/2\pi = 500$ kHz (blue) and by a previous-generation SMPD operated with $\kappa_d/2\pi = 400$ kHz (red). Top: scheme of the experiment. The Er^{3+} spin is magnetically coupled to the microwave field $\vec{B}_1$ of an LC resonator and Zeeman tuned to resonance by a field $\|\vec{B}_0\|$. The spin frequency is set to 7.7492 GHz in the latest version of the experiment and to 7.335 GHz for the "old" version. The spin is excited by a π pulse, and the photon it emits upon radiative relaxation is detected by the SMPD. Graph: blue full circles are the measured count rate following a π-pulse excitation of the spin, as a function of the time, with the SMPD presented herein. The solid blue line is an exponential fit, from which we extract the spin lifetime $\Gamma_R^{-1} = 1.24$ ms and spin-to-click efficiency, $\eta = 0.4$. Note that the noise floor $\alpha_{\rm err} + \alpha_{\rm th} = 0.12$ ms^{-1} is slightly higher than expected from Fig. 4, possibly due to a different wiring scheme in the cryostat. The red full circles and solid line are the equivalent data and fit for the same experiment performed with a previous-generation SMPD. One can observe a fourfold improvement of η from the previous to the newest SMPD generation, yielding a measurement time faster by an order of magnitude.

lower than in the measurements of Fig. 3 and corresponding to a mode temperature of 38 mK. The intercept at $\kappa_d = 0$ is 11.6 s^{-1}, consistent with the error rate $\alpha_{\rm err}$ measured with pump detuned. Overall, the observed linear dependence of $\alpha_{\rm th}$ on κ_d demonstrates that these counts are indeed due to thermal photons impinging on the SMPD input line. Not much can be inferred about their spectrum, apart from the fact that it appears to be flat on the scale of the detection bandwidth (approximately 1 MHz).

For Fig. 4, no data have been taken above $\kappa_d/2\pi = 1$ MHz. Indeed, above this value, high pump amplitudes are required to keep $C = 1$, and our microwave setup was unable to send high enough power.

E. Single-spin measurements

We confirm the high efficiency of the detector by measuring the microwave fluorescence from a single electronic spin. The setup closely follows Refs. [8,40] and is schematically depicted in Fig. 5. The electronic spin is an Er^{3+} ion in a $CaWO_4$ matrix and is coupled to a superconducting resonator to enhance its radiative decay rate Γ_R. The spin is excited by a π pulse with near-unit probability. It then relaxes radiatively by emitting a photon, which is either absorbed by the internal losses of the spin resonator or emitted in the line, after which it may reach the SMPD detector or be absorbed by the losses between the two devices. The SMPD buffer ω_b is tuned to the spin and resonator frequency. The spin-to-click probability is therefore $\eta = \eta_{\rm reso}\eta_{\rm loss}\eta_{\rm SMPD}(\omega_b)$, with $\eta_{\rm reso} = 0.6$ in this device (described in more detail elsewhere [40]).

The spin microwave fluorescence curve is shown in Fig. 5. This is well fitted by an exponential decay with time constant $\Gamma_R^{-1} = 1.24$ ms on top of a constant background, due to the SMPD dark counts. From the integral below the fluorescence curve, we obtain $\eta = 0.4$. This implies that the microwave power absorption between the spin device and the SMPD is $\eta_{\rm loss} = 0.85$, a very plausible value given that the line includes a superconducting cable, a circulator, and an infrared filter. This provides an independent confirmation of the high efficiency reached by this SMPD device and of its relevance for single-spin spectroscopy.

V. CONCLUSION

We have demonstrated a microwave photon counter with tunable frequency (in the 7-GHz range) and bandwidth (between approximately 100 kHz and approximately 1 MHz). The device has a maximum efficiency of 0.8, and its noise level can be reduced by lowering the bandwidth. At an input bandwidth of 200 kHz, we demonstrate a record power sensitivity of 3×10^{-23} W/$\sqrt{\rm Hz}$. The device is well suited to detecting emitters with a narrow line, and it will find applications in single-spin magnetic resonance [40,41] as well as in haloscope-based dark-matter searches [37].

ACKNOWLEDGMENTS

We acknowledge technical support from P. Sénat, D. Duet, P.-F. Orfila, and S. Delprat, and we are grateful for fruitful discussions within the Quantronics group.

We acknowledge support from the Agence Nationale de la Recherche (ANR) through the MIRESPIN (ANR-19-CE47-0011) project. We acknowledge support of the Région Ile-de-France through the DIM QUANTIP, from the AIDAS virtual joint laboratory, and from the France 2030 plan under Grant No. ANR-22-PETQ-0003. This project has received funding from the European Union Horizon 2020 research and innovation program under the OpenSuperQ100+ project, and from the European Research Council under Grant No. 101042315 (INGENIOUS). We acknowledge IARPA and Lincoln Labs for providing the Josephson traveling-wave parametric amplifier.

DATA AVAILABILITY

The data that support the findings of this article are not publicly available upon publication because it is not technically feasible and/or the cost of preparing, depositing, and hosting the data would be prohibitive within the terms of this research project. The data are available from the authors upon reasonable request.

APPENDIX A: PUMP CALIBRATION

In this appendix, we detail the tuning procedure for the pump parameters. The optimal pump frequency should satisfy the 4WM condition, $\omega_{4\mathrm{WM}} = \omega_q + \omega_w - \chi_w - \omega_b$. In the calibration procedure of the device, pump calibration comes after qubit characterization and readout calibration, which results are displayed in Fig. 6.

The pump amplitude is chosen by recording two-dimensional plots such as those shown in Fig. 7, where the qubit excited-state probability is recorded as a function of pump and signal frequency, ω_p and ω, respectively, for various pump powers. Each plot is then fitted to the following formula [42]:

$$|S_{w\leftarrow b}(\delta,\delta_p)|^2 = \frac{4C}{\left|1 + C - 4\frac{\delta(\delta+\delta_p)}{\kappa_b\kappa_w} + 2i\frac{\delta}{\kappa_b} + 2i\frac{\delta+\delta_p}{\kappa_w}\right|^2}, \tag{A1}$$

where $\delta = \omega - \omega_b$ is the signal-buffer detuning, and $\delta_p = \omega_p - \omega_{4\mathrm{WM}}$ the pump detuning from the 4WM condition.

If all detunings are zero, Eq. (A1) becomes

$$|S_{w\leftarrow b}(\delta = 0, \delta_p = 0)|^2 = \frac{4C}{(1+C)^2}. \tag{A2}$$

The maximum of Eq. (A2) is reached for $C = 1$, and its value is 1.

The fit returns the value of C, and after a few iterations, the condition $C = 1$ is readily achieved.

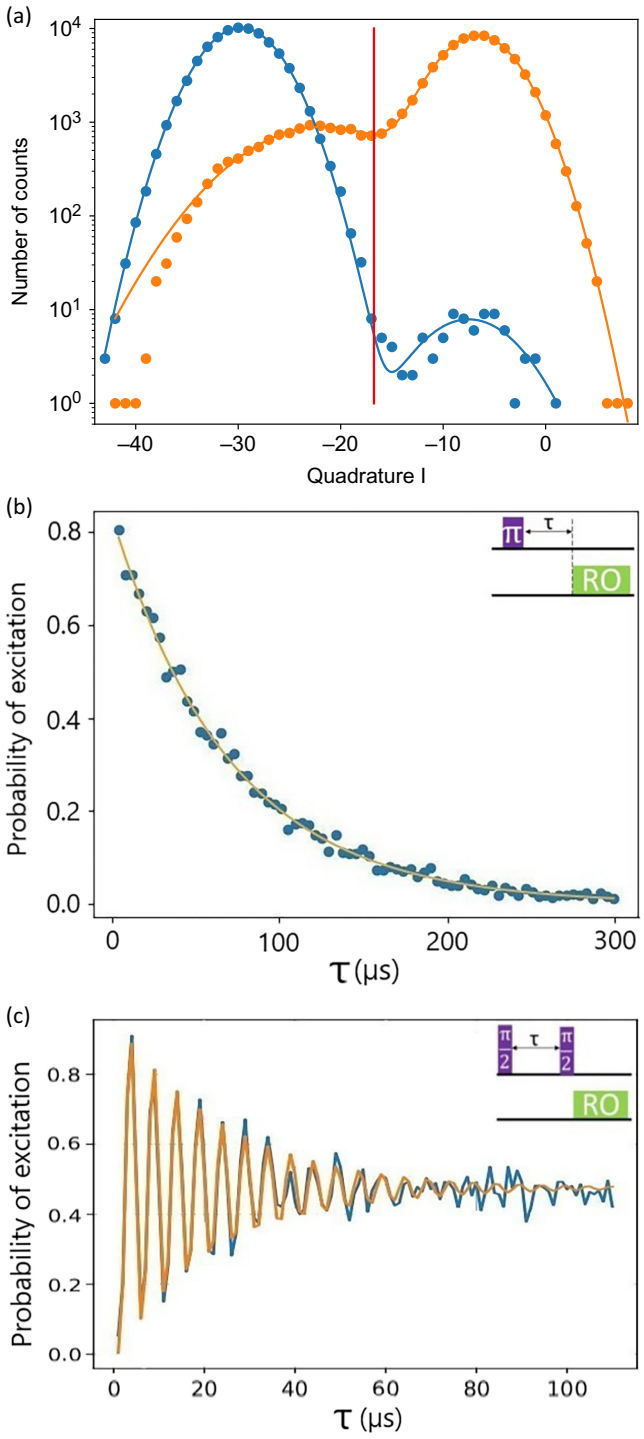


FIG. 6. (a) Qubit readout histograms after 95 650 sequences, in the absence of any preparation pulse (blue full circles) and after a π pulse (orange full circles). Solid lines are fits by a sum of two Gaussians centered on the two I quadrature values corresponding to the ground and excited states, yielding $p_{\mathrm{th},q} = 8.5 \times 10^{-4}$ and $\mathcal{F}_{\mathrm{RO}}^{|e\rangle} = 0.87$. The red line shows the threshold. (b) Qubit excited-state probability following a π pulse, yielding $T_1 = 70$ μs. (c) Qubit Ramsey fringes yielding $T_2^* = 20$ μs. Insets: corresponding pulse sequences. Purple pulses are sent through the drive line, green through the readout (RO) line.

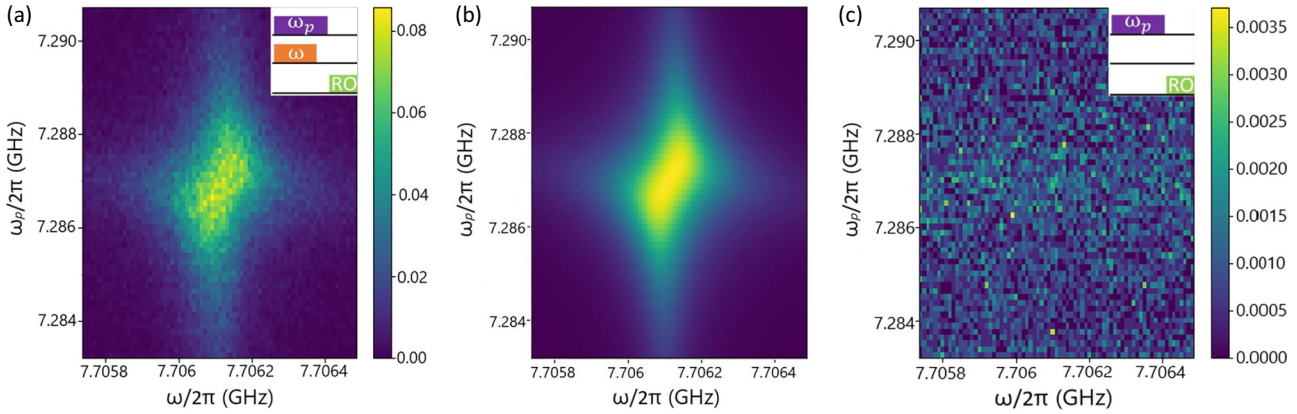


FIG. 7. (a) Four-wave mixing pattern: this color plot shows the measured qubit excited state as a function of pump frequency ω_p and signal frequency ω (from the input line). The qubit is excited only when the signal is close to ω_b, and the pump verifies the 4WM condition. (b) Fit from a two-coupled-cavity model. To fit the data, the value of the cooperativity C is adjusted. Here, the value is $C = 0.99$. Other fit parameters are the buffer linewidth, $\kappa_b/2\pi = 120$ kHz, and the waste linewidth, $\kappa_w/2\pi = 1.75$ MHz. (c) Same experiment as in (a), but with the signal tone switched off. The higher excitation probabilities seen in (a) are no longer visible, demonstrating that we were indeed observing the actual 4WM pattern. Insets: corresponding pulse sequences. Purple pulses are sent through the pump or drive line, orange pulses through the signal or input line, and green pulses through the waste or readout (RO) line. The pumping, signal, and readout pulses are respectively 15-μs, 10.5-μs, and 800-ns long.

Note that the full width at half maximum along the signal frequency axis of $|S_{w\leftarrow b}(\delta,\delta_p)|^2$ is the detection bandwidth of the SMPD:

$$\kappa_d = \sqrt{2}\sqrt{\sqrt{\kappa_b^2\kappa_w^2 + \left(\frac{\kappa_b-\kappa_w}{2}\right)^4} - \left(\frac{\kappa_b-\kappa_w}{2}\right)^2}. \quad \text{(A3)}$$

When $\kappa_b \ll \kappa_w$ (as is the case in this work), the formula can be approximated as

$$\kappa_d \approx 2\kappa_b. \quad \text{(A4)}$$

Figure 8 shows that Eq. (A4) is verified experimentally.

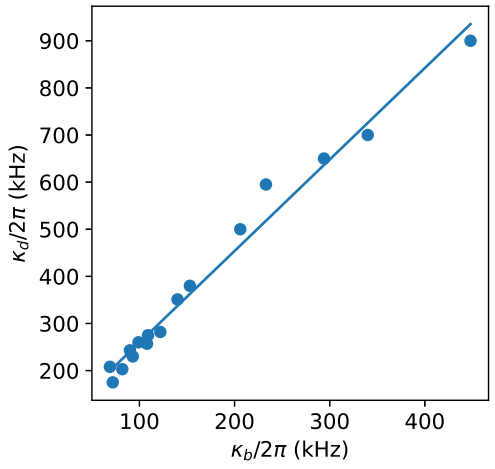


FIG. 8. Detection bandwidth κ_d as a function of buffer bandwidth κ_b. Full blue circles are experimental data and the blue solid line is a linear fit. The fit returns a slope of 1.9, which is close to 2, the value that is expected from Eq. (A4).

APPENDIX B: EFFICIENCY MEASUREMENT

Measuring the efficiency of the SMPD begins with estimating the power at the buffer input. This is achieved by using the qubit itself as a detector. Ramsey fringes are shifted by Δ_q and dephased by Γ_q according to the equation

$$\Delta_q + i\Gamma_q = \frac{-4\chi_b|\epsilon|^2}{(\kappa_b + i\chi_b)^2 + 4\delta^2}, \quad \text{(B1)}$$

where ϵ is the complex amplitude of the intracavity field. The efficiency is then simply computed by dividing the number of clicks per second by the number of photons per second at the device input.

APPENDIX C: SMPD FABRICATION

We now describe the fabrication recipe for the SMPD presented in this paper.

1. Substrate preparation

The process starts with a two-inch (50.8-mm), double-side-polished sapphire wafer. This wafer is dipped in a piranha solution made with 2/3 sulfuric acid and 1/3 hydrogen peroxide (by volume) and left for 20 min. Then, it is rinsed with water and dried with a stream of nitrogen. After that, the wafer is loaded into an rf reactive sputterer together with a tantalum target. The targeted thickness of the tantalum sputtering is between 80 and 90 nm. The sputtering process is performed while the wafer is heated up to 600 °C to obtain alpha-phase tantalum.

The wafer is then prepared for dicing. To this end, UVIII is spin-coated over the wafer for 60 s at 3000 rpm with an acceleration of 2000 rpm/s, followed by a postbake at 120 °C for 3 min.

2. Circuit etching

After dicing, the protective UVIII layer is removed by applying isopropanol (IPA) from a wash bottle to the chosen chip for 15 s, then again for 5 s. For further cleaning, the chip is immersed in acetone under strong ultrasonic agitation for 5 min, then in another ultrasonic bath of IPA for 3 min. It is then dried with a stream of nitrogen and immersed in a piranha solution for 20 min. The chip is then rinsed with water, dehydrated with IPA, dried with a stream of nitrogen, and further dehydrated on a hotplate at 120 °C for 5 min. Next, AZ1518 is spin-coated for 60 s at 3000 rpm with an acceleration of 2000 rpm/s. The postbake is performed on a hotplate for 2 min at 115 °C. The circuit is then patterned using a UV laser direct writer. A supplementary exposure is needed at the edge bead. The development is performed in pure MF319 for 60 s and stopped with water. The chip is dried with a stream of nitrogen and hard baked on a hotplate for 2 min at 115 °C. Finally, the circuit is etched by dipping in Transene 111 (1/3 nitric acid, 1/3 hydrofluoric acid, and 1/3 water) for exactly 20 s. There is no need for agitation during etching. Rinsing is performed in a first bath of water for 20 s with agitation and then in a second bath of water for transport between benches.

3. Chip cleaning and oxide removal

After the etching step, the chip is recleaned before proceeding to the e-beam-related steps. Recently, we added an oxide-removal step to the process, which has not been applied to the sample presented here. First, the sample is immersed in a bath of acetone for 5 min to remove AZ1518, then in another bath of IPA for 3 min, and finally in piranha solution for 2 min. The chip is rinsed with water, dehydrated with IPA, and dried with a stream of nitrogen.

In the recently added oxidation step, the chip is immersed for 20 min in buffered oxide etchant, rinsed in a first bath of water for 20 s with agitation, then in a second bath of water for transport between benches, dehydrated with IPA, dried with a stream of nitrogen, and further dehydrated on a hotplate for 5 min at 120 °C.

4. Preparation of e-beam bilayer

A first layer of MAA EL-6 is spin-coated for 60 s at 4000 rpm with an acceleration of 1000 rpm/s. The postbake is performed on a hotplate for 5 min at 172 °C. This is followed by spin coating a second layer of PMMA 950k A6 for 60 s at 3000 rpm with an acceleration of 2000 rpm/s. The postbake, on a hotplate at 175 °C, lasts 15 min.

The substrate being made of sapphire, there is no way for electrons to escape through it during lithography. Therefore, the bilayer must be metallized to prevent charge effects. For this reason, a 7-nm-thick layer of aluminum is evaporated over the bilayer at a rate of 0.2 nm/s. There is no need for a good vacuum for this evaporation step; a pressure of about 10^{-6} hPa is enough.

5. E-beam lithography

Given the need for the simultaneous presence of Josephson junctions of very different sizes across the device, the Manhattan process has been chosen. Due to the absence of a 100-kV electron-beam lithography system in our laboratory, we developed an adapted version of this process using a bilayer with a reversed aspect ratio (a layer of MAA about 170-nm thick beneath a layer of PMMA about 580-nm thick). We use the following parameters with our Raith e-LINE system:

(1) Magnification: $\times 1000$.
(2) Base dose: 250 $\mu C/cm^2$.
(3) Relative dose factor: 1.5 for "big" junctions' main pattern (about 1 μm edge size), 1.7 for "small" junctions' main pattern (about 200 nm edge size or less), 0.3 for undercut boxes.
(4) Voltage: 25 kV.
(5) Aperture: 10 μm.
(6) Current: About 20 pA.
(7) Write field: 100×100 μm^2.

6. Aluminum etching, resist development, and descum

Before developing the e-beam resist, the metallization layer must be removed. Aluminum etching is performed by dipping the chip in a 10 g/l potassium hydroxide (KOH) solution in water for 30 s. It is then rinsed by dipping for 3 s in water, followed by 3 s in IPA. The development itself begins immediately after: the chip is immersed for 45 s in a solution made of 1/4 methyl isobutyl ketone (MIBK) and 3/4 IPA (by volume). Development is stopped by dipping in IPA for 15 s. The chip and the bilayer are dried first with a stream of nitrogen, then on a hotplate at 70 °C for 1 min. Finally, the resist mask is cleaned in an oxygen plasma asher for 10 s, at a pressure of 0.2 hPa and an ionizing power of 75 W.

7. Josephson-junction evaporation

For evaporating Josephson junctions, a good vacuum is required (at least below 5×10^{-7} hPa). Given that we are using the Manhattan process, the evaporator must be equipped with a planetary rotation. The parameters given here apply to one of our Plassys MEB 550S systems.

First, the surface is prepared by argon-ion milling with an incidence angle of 0°. The ion gun is tuned with the filament at 500 V and 25 mA, and the acceleration grid

at 100 V. The shutter is removed from the ion-beam trajectory twice for 5 s each, with 1 min of rest between exposures. Then comes the evaporation of the first layer of aluminum, performed at an angle of 30° and a rate of 1 nm/s. A thickness of 29 nm is set on the evaporator to obtain an actual thickness of 25 nm. This first layer is oxidized by a mixture of oxygen and argon at 10 hPa for 5 min. The sample holder is rotated around the planetary axis by 90° to evaporate along the orthogonal direction of the Manhattan pattern. Finally, the second evaporation of aluminum is performed with the same parameters (30° angle and 1 nm/s rate), except that a thickness of 69 nm is set to get an actual thickness of 60 nm.

8. Final lift off

The lift off is performed in two successive baths of acetone at 60 °C. Blowing with a Pasteur pipette helps with

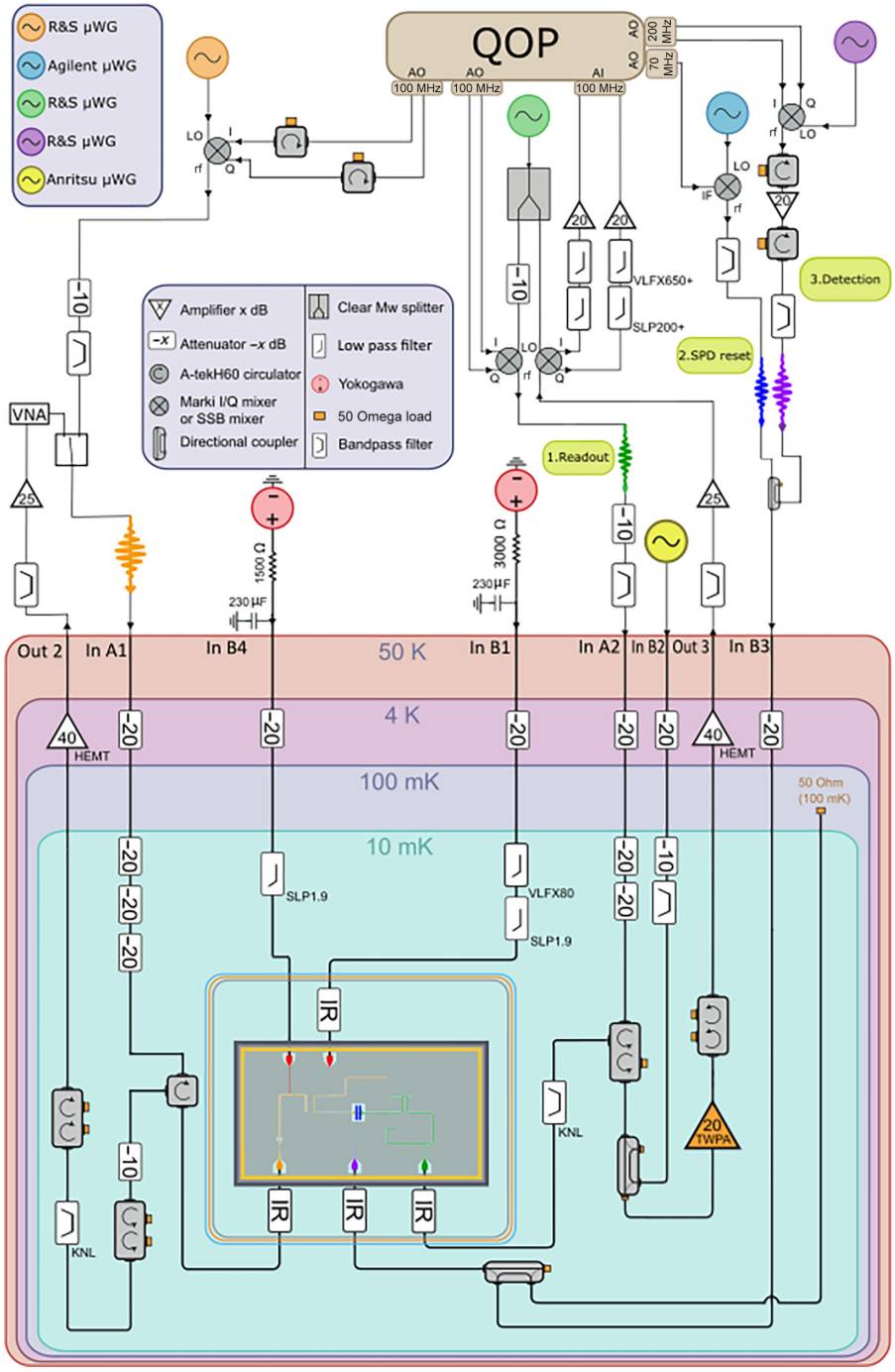


FIG. 9. Wiring used for the characterization run reported herein.

removal. The sample is then brought back to room temperature in a non-heated bath of acetone. It is then dehydrated in IPA and finally dried with a stream of nitrogen.

APPENDIX D: WIRING DIAGRAM

The wiring scheme used for SMPD characterization is presented in Fig. 9. Lines "In A1" and "Out 2" are used to probe the buffer resonator in reflection (to determine ω_b and κ_b), and also to calibrate the detector efficiency by sending pulses containing a well-controlled number of photons. "In B1" and "In B4" are flux bias lines for controlling the SQUID inductances of the buffer and its Purcell resonator, respectively. "In A2" and "Out 3" are used for probing the waste resonator in reflection (to determine ω_w and κ_w), and also to perform dispersive readout of the qubit through the waste resonator. "In B2" is used to pump the traveling-wave parametric amplifier (TWPA) on the "Out 3" line. "In B3" is the qubit drive line.

[1] M. Orrit and J. Bernard, Single pentacene molecules detected by fluorescence excitation in a p-terphenyl crystal, Phys. Rev. Lett. **65**, 2716 (1990).

[2] T. A. Klar, S. Jakobs, M. Dyba, A. Egner, and S. W. Hell, Fluorescence microscopy with diffraction resolution barrier broken by stimulated emission, Proc. Natl. Acad. Sci. U.S.A. **97**, 8206 (2000).

[3] E. Betzig, G. H. Patterson, R. Sougrat, O. W. Lindwasser, S. Olenych, J. S. Bonifacino, M. W. Davidson, J. Lippincott-Schwartz, and H. F. Hess, Imaging intracellular fluorescent proteins at nanometer resolution, Science (New York, N.Y.) **313**, 1642 (2006).

[4] C. Bruschini, H. Homulle, I. M. Antolovic, S. Burri, and E. Charbon, Single-photon avalanche diode imagers in biophotonics: Review and outlook, Light Sci. Appl. **8**, 87 (2019).

[5] N. Gisin, G. Ribordy, W. Tittel, and H. Zbinden, Quantum cryptography, Rev. Mod. Phys. **74**, 145 (2002).

[6] L. Banchi, M. Fingerhuth, T. Babej, C. Ing, and J. M. Arrazola, Molecular docking with Gaussian boson sampling, Sci. Adv. **6**, eaax1950 (2020).

[7] E. Albertinale, L. Balembois, E. Billaud, V. Ranjan, D. Flanigan, T. Schenkel, D. Estéve, D. Vion, P. Bertet, and E. Flurin, Detecting spins by their fluorescence with a microwave photon counter, Nature **600**, 434 (2021).

[8] Z. Wang, L. Balembois, M. Rančić, E. Billaud, M. Le Dantec, A. Ferrier, P. Goldner, S. Bertaina, T. Chaneliére, D. Esteve, D. Vion, P. Bertet, and E. Flurin, Single-electron spin resonance detection by microwave photon counting, Nature **619**, 276 (2023).

[9] E. Billaud, L. Balembois, M. Le Dantec, M. Rančić, E. Albertinale, S. Bertaina, T. Chaneliére, P. Goldner, D. Estéve, D. Vion, P. Bertet, and E. Flurin, Microwave fluorescence detection of spin echoes, Phys. Rev. Lett. **131**, 100804 (2023).

[10] S. K. Lamoreaux, K. A. van Bibber, K. W. Lehnert, and G. Carosi, Analysis of single-photon and linear amplifier detectors for microwave cavity dark matter axion searches, Phys. Rev. D **88**, 035020 (2013).

[11] A. V. Dixit, S. Chakram, K. He, A. Agrawal, R. K. Naik, D. I. Schuster, and A. Chou, Searching for dark matter with a superconducting qubit, Phys. Rev. Lett. **126**, 141302 (2021).

[12] M. Scigliuzzo, A. Bengtsson, J.-C. Besse, A. Wallraff, P. Delsing, and S. Gasparinetti, Primary thermometry of propagating microwaves in the quantum regime, Phys. Rev. X **10**, 041054 (2020).

[13] R. Assouly, R. Dassonneville, T. Peronnin, A. Bienfait, and B. Huard, Quantum advantage in microwave quantum radar, Nat. Phys. **19**, 1418 (2023).

[14] R. Raussendorf, D. E. Browne, and H. J. Briegel, Measurement-based quantum computation on cluster states, Phys. Rev. A **68**, 022312 (2003).

[15] H. J. Briegel, D. E. Browne, W. Dür, R. Raussendorf, and M. Van den Nest, Measurement-based quantum computation, Nat. Phys. **5**, 19 (2009).

[16] S. Bartolucci, P. Birchall, H. Bombin, H. Cable, C. Dawson, M. Gimeno-Segovia, E. Johnston, K. Kieling, N. Nickerson, M. Pant, F. Pastawski, T. Rudolph, and C. Sparrow, Fusion-based quantum computation, arXiv:2101.09310v1.

[17] A. Narla, S. Shankar, M. Hatridge, Z. Leghtas, K. M. Sliwa, E. Zalys-Geller, S. O. Mundhada, W. Pfaff, L. Frunzio, R. J. Schoelkopf, and M. H. Devoret, Robust concurrent remote entanglement between two superconducting qubits, Phys. Rev. X **6**, 031036 (2016).

[18] A. Opremcak, I. V. Pechenezhskiy, C. Howington, B. G. Christensen, M. A. Beck, E. Leonard, J. Suttle, C. Wilen, K. N. Nesterov, G. J. Ribeill, T. Thorbeck, F. Schlenker, M. G. Vavilov, B. L. T. Plourde, and R. McDermott, Measurement of a superconducting qubit with a microwave photon counter, Science **361**, 1239 (2018).

[19] J.-C. Besse, S. Gasparinetti, M. C. Collodo, T. Walter, A. Remm, J. Krause, C. Eichler, and A. Wallraff, Parity detection of propagating microwave fields, Phys. Rev. X **10**, 011046 (2020).

[20] R. Lescanne, S. Deléglise, E. Albertinale, U. Réglade, T. Capelle, E. Ivanov, T. Jacqmin, Z. Leghtas, and E. Flurin, Irreversible qubit-photon coupling for the detection of itinerant microwave photons, Phys. Rev. X **10**, 021038 (2020).

[21] G. Romero, J. J. García-Ripoll, and E. Solano, Microwave photon detector in circuit QED, Phys. Rev. Lett. **102**, 173602 (2009).

[22] F. Helmer, M. Mariantoni, E. Solano, and F. Marquardt, Quantum nondemolition photon detection in circuit QED and the quantum Zeno effect, Phys. Rev. A **79**, 052115 (2009).

[23] S. R. Sathyamoorthy, L. Tornberg, A. F. Kockum, B. Q. Baragiola, J. Combes, C. M. Wilson, T. M. Stace, and G. Johansson, Quantum nondemolition detection of a propagating microwave photon, Phys. Rev. Lett. **112**, 093601 (2014).

[24] O. Kyriienko and A. S. Sørensen, Continuous-wave single-photon transistor based on a superconducting circuit, Phys. Rev. Lett. **117**, 140503 (2016).

[25] S. R. Sathyamoorthy, T. M. Stace, and G. Johansson, Detecting itinerant single microwave photons, C. R. Phys. **17**, 756 (2016).

[26] X. Gu, A. F. Kockum, A. Miranowicz, Y.-x. Liu, and F. Nori, Microwave photonics with superconducting quantum circuits, Phys. Rep. **718-719**, 1 (2017).
[27] B. Royer, A. L. Grimsmo, A. Choquette-Poitevin, and A. Blais, Itinerant microwave photon detector, Phys. Rev. Lett. **120**, 203602 (2018).
[28] Y.-F. Chen, D. Hover, S. Sendelbach, L. Maurer, S. T. Merkel, E. J. Pritchett, F. K. Wilhelm, and R. McDermott, Microwave photon counter based on Josephson junctions, Phys. Rev. Lett. **107**, 217401 (2011).
[29] K. Koshino, K. Inomata, T. Yamamoto, and Y. Nakamura, Implementation of an impedance-matched λ system by dressed-state engineering, Phys. Rev. Lett. **111**, 153601 (2013).
[30] K. Inomata, Z. Lin, K. Koshino, W. D. Oliver, J.-S. Tsai, T. Yamamoto, and Y. Nakamura, Single microwave-photon detector using an artificial Λ-type three-level system, Nat. Commun. **7**, 12303 (2016).
[31] J.-C. Besse, S. Gasparinetti, M. C. Collodo, T. Walter, P. Kurpiers, M. Pechal, C. Eichler, and A. Wallraff, Single-shot quantum nondemolition detection of individual itinerant microwave photons, Phys. Rev. X **8**, 021003 (2018).
[32] S. Kono, K. Koshino, Y. Tabuchi, A. Noguchi, and Y. Nakamura, Quantum non-demolition detection of an itinerant microwave photon, Nat. Phys. **14**, 546 (2018).
[33] C. H. Wong and M. G. Vavilov, Quantum efficiency of a single microwave photon detector based on a semiconductor double quantum dot, Phys. Rev. A **95**, 012325 (2017).
[34] A. Ghirri, S. Cornia, and M. Affronte, Microwave photon detectors based on semiconducting double quantum dots, Sensors **20**, 4010 (2020).
[35] G.-H. Lee, D. K. Efetov, W. Jung, L. Ranzani, E. D. Walsh, T. A. Ohki, T. Taniguchi, K. Watanabe, P. Kim, D. Englund, and K. C. Fong, Graphene-based Josephson junction microwave bolometer, Nature **586**, 42 (2020).
[36] L. Balembois, J. Travesedo, L. Pallegoix, A. May, E. Billaud, M. Villiers, D. Estève, D. Vion, P. Bertet, and E. Flurin, Cyclically operated microwave single-photon counter with sensitivity of 10^{-22} W/$\sqrt{\text{Hz}}$, Phys. Rev. Appl. **21**, 014043 (2024).
[37] C. Braggio, L. Balembois, R. Di Vora, Z. Wang, J. Travesedo, L. Pallegoix, G. Carugno, A. Ortolan, G. Ruoso, U. Gambardella, D. D'Agostino, P. Bertet, and E. Flurin, Quantum-enhanced sensing of axion dark matter with a transmon-based single microwave photon counter, Phys. Rev. X **15**, 021031 (2025).
[38] A. Blais, A. L. Grimsmo, S. Girvin, and A. Wallraff, Circuit quantum electrodynamics, Rev. Mod. Phys. **93**, 025005 (2021).
[39] T. Walter, P. Kurpiers, S. Gasparinetti, P. Magnard, A. Potočnik, Y. Salathé, M. Pechal, M. Mondal, M. Oppliger, C. Eichler, and A. Wallraff, Realizing rapid, high-fidelity, single-shot dispersive readout of superconducting qubits, Phys. Rev. Appl. **7**, 054020 (2017).
[40] J. Travesedo, J. O'Sullivan, L. Pallegoix, Z. W. Huang, P. Hogan, P. Goldner, T. Chaneliere, S. Bertaina, D. Esteve, P. Abgrall, D. Vion, E. Flurin, and P. Bertet, All-microwave readout, spectroscopy, and dynamic polarization of individual nuclear spins in a solid, Sci. Adv. **11**, eadu0581 (2025).
[41] J. O'Sullivan, J. Travesedo, L. Pallegoix, Z. Huang, P. Hogan, P. Goldner, D. Esteve, D. Vion, P. Bertet, and E. Flurin, Individual solid-state nuclear spin qubits with coherence exceeding seconds, Nat. Phys. **21**, 1794 (2025).
[42] E. Albertinale, Measuring spin fluorescence with a microwave photon detector, Ph.D. thesis, Université Paris-Saclay (2021).